Annals of Nuclear Energy 224 (2025) 111676

Contents lists available at ScienceDirect

Annals of Nuclear Energy

journal homepage: www.elsevier.com/locate/anucene

A quasi-differential measurement of neutron scattering from tantalum between 0.65 MeV and 20 MeV

Gregory J. Siemers [a,*], Yaron Danon [a], Sukhjinder Singh [a], Katelyn C. Keparutis [a], Peter J. Brain [a,1], Benjamin H. Wang [a], Adam M. Daskalakis [b], Devin P. Barry [b], Michael J. Rapp [b], Robert C. Block [a,2]

[a] Gaerttner LINAC Center, Rensselaer Polytechnic Institute, 3021 Tibbits Ave., Troy, NY, 12180, USA
[b] Naval Nuclear Laboratory, P.O. Box 1072, Schenectady, NY, 12301, USA

ARTICLE INFO

Keywords:
Tantalum
Nuclear data
Validation
Neutron scattering
Angular distributions
Double-differential cross sections

ABSTRACT

Quasi-differential neutron scattering measurements of elemental tantalum (Ta) and carbon were performed at the Gaerttner Linear Accelerator Center at Rensselaer Polytechnic Institute using neutron time-of-flight spectroscopy. An array of eight EJ-301 organic liquid scintillator detectors measured neutron interactions between the pulsed white neutron source and the samples of interest. Signals were converted to digital pulses using a new 10-bit Struck SIS-3305 digitizer, which enhanced neutron detection efficiency above 3 MeV over previous measurements. An improved pulse shape analysis technique was developed and used to discriminate between incident neutron and photon interactions with the scintillator. Neutron time-of-flight histograms were compared with detailed Monte Carlo radiation transport simulations using MCNP6.3. The elemental carbon measurement was reproduced well by the ENDF/B-VIII.0 carbon evaluation, thus verifying the experimental methods and simulation geometry, and providing a normalization to the experimental data. The average deviation between the carbon measurement and evaluation, 4.0%, was adopted as the systematic uncertainty of the experiment. Evaluated neutron scattering and emission data of ^{181}Ta from the ENDF/B-VIII.0, JEFF-3.3, ENDF/B-VIII.1, JENDL-5.0, and TENDL-2023 (updated) libraries were compared with the Ta measurement. The ENDF/B-VIII.0, JEFF-3.3, and TENDL-2023u ^{181}Ta evaluations significantly overpredict Ta neutron scattering between 0.75 MeV and 2.5 MeV at backward scattering angles. In contrast, the ENDF/B-VIII.1 ^{181}Ta evaluation slightly underpredicts the experimental data in this energy range at all measured angles. Generally good agreement is observed between all evaluations and the experimental data above 5 MeV at all angles. The JENDL-5.0 and ENDF/B-VIII.1 ^{181}Ta evaluations show the best agreement with the experimental findings.

1. Introduction

Nuclear data are required to simulate the behavior of radiation traveling through matter. Incident radiation interact differently with all nuclei, therefore experiments are required to observe and tabulate these interactions for computational use. Producing accurate nuclear data with low uncertainty is essential for performing trustworthy radiation transport simulations. The advancement of nuclear data unilaterally supports the progression of many nuclear engineering disciplines, such as reactor design, nuclear non-proliferation and safeguards, dosimetry, and criticality safety.

Multiple organizations maintain and improve libraries of evaluated nuclear data utilized by radiation transport codes, which contain results from theoretical physics models used to best match experimental nuclear data. Some major nuclear data libraries include the US Evaluated Nuclear Data File (ENDF/B-VIII.0) library by Brown et al. (2018), the Joint European Fission and Fusion (JEFF-3.3) library by Plompen et al. (2020), the Japanese Evaluated Nuclear Data Library (JENDL-5.0) by Iwamoto et al. (2023), and the International Atomic Energy Agency's (IAEA) TALYS Evaluated Nuclear Data Library (TENDL-2023u) by Koning et al. (2019). Evaluated nuclear data within these libraries often agree for a given isotope; however, differences in the interpretation of experimental nuclear reaction data and/or physics models used to represent the measured data can lead to discrepancies. In this work, the differences in evaluated tantalum (Ta) nuclear datasets, particularly the

* Corresponding author.
E-mail address: siemeg@rpi.edu (G.J. Siemers).
[1] Now at: Los Alamos National Laboratory, Los Alamos, NM 87544.
[2] Retired.

https://doi.org/10.1016/j.anucene.2025.111676
Received 17 March 2025; Received in revised form 5 May 2025; Accepted 17 June 2025
Available online 16 July 2025

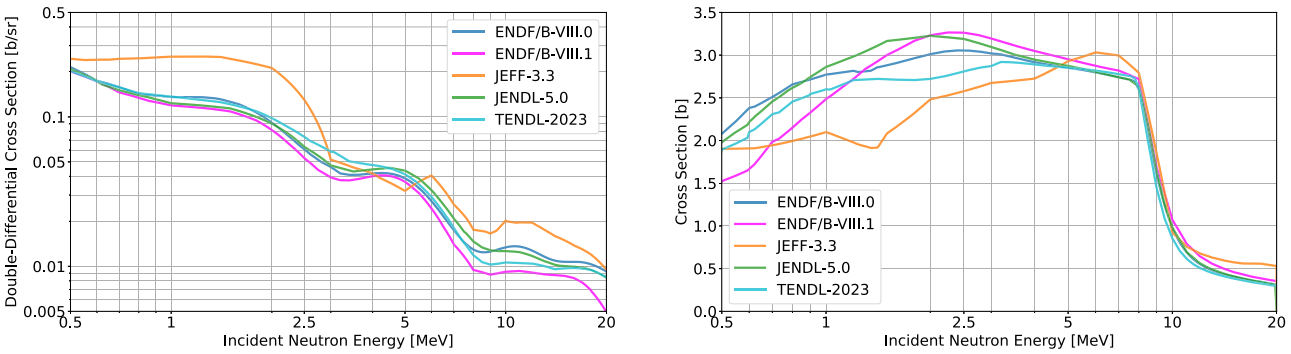

Fig. 1. (a) Double-Differential elastic scattering cross sections, $\frac{d\sigma}{d\Omega}(E)$, of ^{181}Ta at 110 degrees available in major evaluated nuclear data libraries. (b) ^{181}Ta inelastic scattering cross sections, $\sigma_{inl}(E)$, available in major evaluated nuclear data libraries.

^{181}Ta isotope which comprises 99.99% of elemental Ta (Meija et al., 2016), are investigated. Fig. 1 illustrates the differences in both the double-differential elastic scattering, $\frac{d\sigma}{d\Omega}(E)$, and the integral inelastic scattering cross sections between several evaluated ^{181}Ta nuclear datasets.

Tantalum is a refractory metal that has a desirable combination of chemical, mechanical, and neutronic properties for applications in nuclear engineering. It exhibits excellent resistance to thermal and mechanical stresses, with a melting point of 3269 K (Malter and Langmuir, 1939), and is resistant to many corrosives (Taylor, 1999). Thus, tantalum is often utilized to fabricate components that must withstand extreme environments. In particular, tantalum is used as neutron-producing targets at electron linear accelerator facilities, such as the Gaerttner Linear Accelerator Center at Rensselaer Polytechnic Institute (RPI), and as crucibles for handling molten actinides (Sakamura et al., 1998 and Spirlet et al., 1985). The latter of which can raise criticality safety concerns when handing substantial quantities of fissile actinides.

Recently, many efforts have been made to reduce criticality safety concerns surrounding the use of tantalum. Contributions include designing and performing new integral benchmark experiments (Percher, 2019 and Hutchinson et al., 2024) and new differential neutron transmission and radiative capture measurements (Rapp et al., 2019, Brown et al., 2019, McDermott, 2016, and Brown et al., 2023). These new experiments have been used to produce a new resolved resonance region (RRR) evaluation by Barry et al. (2024), an unresolved resonance region (URR) evaluation by Brown et al. (2025), and a high-energy region evaluation by Herman and Kowano (2021) for the release of the ENDF/B-VIII.1 nuclear data library (Nobre et al., 2025). The measurement performed in this work aims to provide an independent, *post hoc*, performance validation of the high energy region of the new ENDF/B-VIII.1 ^{181}Ta incident neutron evaluation. And to provide insight into areas in which all the ^{181}Ta evaluations investigated can be improved.

2. Theory

The quasi-differential neutron time-of-flight measurement presented in this manuscript utilized organic liquid scintillator radiation detectors to observe neutron-induced neutron emissions from tantalum. For a non-fissionable sample, such as Ta, the measured neutron emissions are dominated by elastic and inelastic neutron scattering reactions with the target nucleus. Neutrons emitted from other decay channels, such as (n,2n) or (n,np), are present as the incident neutron energy increases beyond the neutron separation energy, which is 7.5768(14) MeV for ^{181}Ta (Wang et al., 2012). Despite this, the measured quantity from this experiment will be referred to as quasi-differential neutron scattering. This quantity represents the number of neutrons with initial energy E which underwent either a single or multiple neutron scattering and/or emitting reaction(s) within the Ta sample, and escaped in the direction of a neutron detector θ, with a new energy E'. Note that only neutrons with a sufficiently high E', about 400 keV, are detected. The reader who is interested in the mathematical representation of the measured quantity is directed to those presented by Saglime (2009).

The likelihood that a neutron with energy, E, undergoes a particular nuclear interaction, x, with a target nucleus is defined as a cross section, $\sigma_x(E)$. The angular distributions of particles emitted following a nuclear interaction are often represented as Legendre polynomial expressions, $f(\mu)$, where μ is the cosine of angle by which the outgoing particle is emitted, θ. These nuclear reaction cross sections and angular distributions are required to solve the neutron transport equation, such as the linear Boltzman transport equation,

$$\frac{1}{v}\frac{\delta\Psi}{\delta t}(\vec{r},\vec{\Omega},E,t)+\vec{\Omega}\cdot\nabla\Psi(\vec{r},\vec{\Omega},E,t)+\Sigma_t(E)\Psi(\vec{r},\vec{\Omega},E,t)= \int_0^\infty\int_{4\pi}\Sigma_s(\overrightarrow{\Omega'}\cdot\vec{\Omega},E'\rightarrow E)\Psi(\vec{r},\overrightarrow{\Omega'},E',t)d\Omega' dE'+\frac{Q(\vec{r},E,t)}{4\pi}, \quad (1)$$

in a radiation transport code. Here, various nuclear reaction cross sections, such as $\Sigma_t(E)$ and $\Sigma_s(\overrightarrow{\Omega'}\cdot\vec{\Omega},E'\rightarrow E)$, are highlighted in red. Solutions obtained from Eq. (1) are therefore dependent on the nuclear reaction cross section and angular distribution data utilized when performing the calculation. Producing the evaluated nuclear reaction data needed for these calculations is difficult, particularly in the MeV energy region, where many modes of decay are competing in the neutron-nucleus system, several nuclear reaction kinematic mechanisms are occurring, and available experimental nuclear data are sparse. Quasi-differential neutron scattering measurements, including this work, uniquely provide experimental nuclear reaction data to constrain optical model parameters and Hauser–Feshbach statistical calculations when modeling high energy nuclear reactions, or a *post hoc* performance validation of existing evaluated nuclear reaction data.

3. Experimental configuration

3.1. RPI linear accelerator center

The neutron time-of-flight experiments presented in this work were performed at the Gaerttner Linear Accelerator (LINAC) center at RPI. The accelerator is capable of accelerating bunches of electrons to ~50 MeV, which are incident on a tantalum target. These high energy electrons slow down in the tantalum target creating bremsstrahlung photons. Then, through the Ta photoneutron (γ,n) reaction, a nearly isotropic pulsed white neutron source is produced, and used for neutron time-of-flight spectroscopy. For this experiment, the LINAC was pulsed at a repetition rate of 400 Hz with an electron burst width of 8 ns and an average current of ~11 μA. The unmoderated, or bare-bounce, tantalum target (Overberg et al., 1999) was used to maximize the neutron

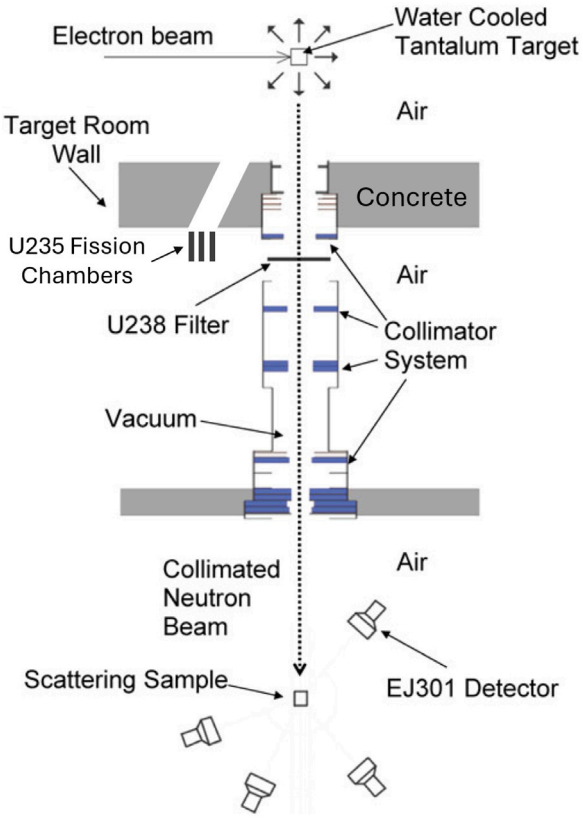

Fig. 2. Illustration of the experimental setup for performing high energy quasi-differential neutron scattering measurements using the time-of-flight technique at the RPI LINAC Center. This figure is not to scale.

flux in the high keV and MeV neutron energy region. Various steel, lead, and B_4C collimators present within the evacuated flight tubes of the west neutron beamline, illustrated in Saglime (2009), reduced the neutron beam diameter to 3 inches at the sample location, 30.07 meters downstream from the neutron-producing Ta target. Additionally, a 0.987 inch ± 0.012 inch depleted uranium (DU) filter was placed in the beam to reduce the intensity of the bremsstrahlung gamma flash. Finally, fluctuations in the neutron beam intensity were measured continuously during the experiment by three ^{235}U fission chambers. The fission chambers are located approximately 9 meters downstream from the neutron-producing Ta target on an isolated flight path, and are moderated with high-density polyethylene (HDPE). Fig. 2 provides an illustration the high energy neutron scattering time-of-flight experimental setup at RPI.

3.2. RPI high energy neutron scattering system

The RPI high energy neutron scattering system (Fig. 3) was developed to measure neutron scattering and other neutron/photon emissions from samples of interest in the high keV and MeV energy region by Saglime et al. (2010). The detector system employs an array of eight 5 inch diameter by 3 inch depth organic liquid scintillator detectors manufactured by Eljen Technology (2021), type 301 (EJ-301). These detectors are coupled to 5 inch diameter Photonis XP45720-B photomultiplier tubes (PMT). The high voltage was supplied to the PMTs by a (CAEN, 2005) power supply unit (model 1733N) housed within a SYS3527 chassis; amplifying the scintillation light produced by incident radiation. The electrical signals from the PMTs were then converted to digital pulses using a 10-bit Struck SIS-3305 digitizer. The EJ-301 detectors can be positioned at various angles around the scattering sample and are rigidly held in place by aluminum supports,

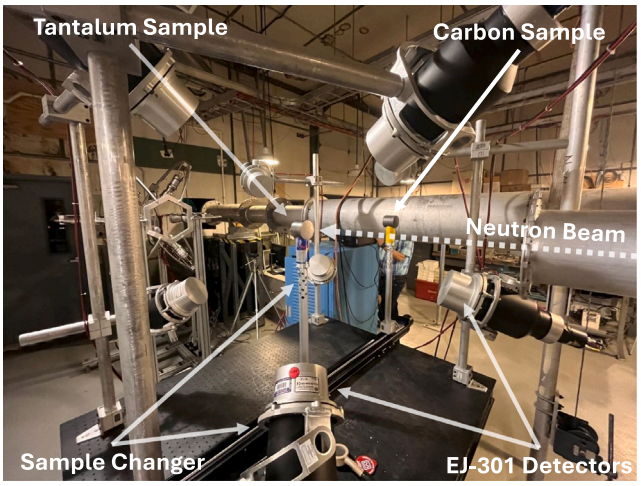

Fig. 3. The RPI high energy neutron scattering system. The tantalum and carbon samples measured in this work are present on the left and right sample holders, respectively. The center of the sample is located 30.07 meters downstream from the neutron producing target.

mounted to a 5-foot by 4-foot optical table. Several structural upgrades were made to the RPI high energy neutron scattering system prior to performing these measurements. Most notably, custom aluminum (type 6061) reinforcements and adapters were added to the low-mass sample holders, which more rigidly fastened each to the sample changer. These updates reduced the likelihood of sample position fluctuations over the course of the measurement, in turn reducing a potential source of systematic uncertainty of the experiment.

3.3. Upgrade to a 10-bit digitizer

A substantial upgrade to the pulse digitization capability of the RPI high energy neutron scattering system was performed during this work. Previously, electrical signals from the PMTs were converted into digital waveforms using an 8-bit Agilent-Acqiris AP240 digitizer (Saglime, 2009, Barry et al., 2013, Daskalakis, 2015, Blain et al., 2022, and Youmans et al., 2015). For this work, the digitization system was upgraded to a (Struck Innovate Systeme, 2024) 10-bit SIS-3305 digitizer. This digitizer increased both the dynamic range in which pulses could be digitized from 256 bits to 1024 bits, and the sampling rate of a pulse from 1 ns to 0.8 ns. These enhancements lead to an increase in the relative neutron detection efficiency of the system above 3 MeV compared to the 8-bit Acqiris system (Fig. 4) since larger pulses could now be fully resolved. The decreased efficiency below 1 MeV is attributed to the lower gain, 1060 V on average, applied to the PMTs to accommodate the lower acceptance voltage range of pulses using the SIS-3305 digitizer (1.5 V) compared to the 8-bit Acqiris (5 V). Details for how the relative neutron detection efficiency is determined are discussed in Section 4.2.1.

4. Methods

The quasi-differential method was developed at RPI to investigate the performance of evaluated neutron scattering and emission data. The method leverages robust Monte Carlo radiation transport techniques, a detailed experimental geometry, and validated measurements of the incident neutron flux on the sample. The samples measured during these experiments are relatively thick allowing for multiple collisions to occur. This choice increases the signal to the neutron detectors, and subsequently decreases the statistical uncertainty of the measurement. This is contrary to double-differential cross section or angular distribution measurements, such as those conducted by Smith and Guenther

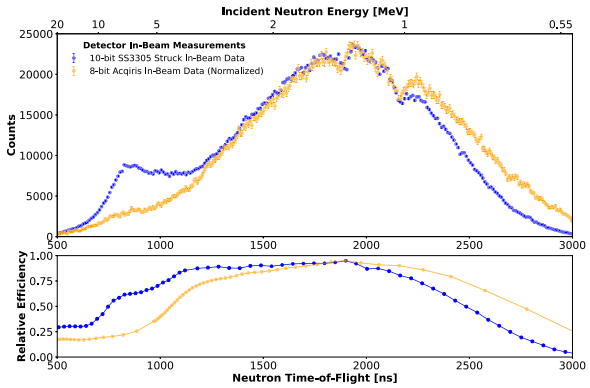

Fig. 4. Comparison of relative neutron detection efficiency measurements between systems using an 8-bit and 10-bit digitizer. The peak of 8-bit has been normalized to the peak 10-bit data. The 8-bit data were collected by Daskalakis et al. (2014).

(1982), which require very thin, isotopically enriched samples. The measurements performed in this work are thus quasi-differential and are particularly well suited for validating the holistic performance of neutron-emitting reaction channels in nuclear data evaluations.

The quasi-differential method includes performing neutron time-of-flight measurements on a well-known reference material (typically elemental carbon), a sample of interest, and of the open beam (LINAC-induced background). Additional neutron time-of-flight experiments are required to measure the incident neutron flux profile on the sample, and the relative neutron detection efficiency of each EJ-301 detector. The measured neutron scattering time-of-flight histograms of the reference measurement are first compared to detailed radiation transport simulations using the Monte Carlo N-Particle[3] transport code, version 6.3 (`MCNP6.3`) (Rising et al., 2023), to validate the experimental geometry, determine a normalization factor to the experimental data, and estimate the systematic uncertainty of the experiment. Then, radiation transport simulations of the sample of interest are performed using various evaluated nuclear data libraries, normalized to the experimental data using the aforementioned normalization factor, and their respective performance investigated. Previous experiments using this technique have been used to resolve issues in various nuclear data evaluations, such as beryllium (Be) by Daskalakis (2023), Pb by Brain (2023), and ^{238}U by Capote et al. (2014).

4.1. Data processing and analysis

For these experiments, electrical signals corresponding to measured neutron and photon radiation were converted into digital pulses by a Struck SIS-3305 digitizer and stored in binary files. The amplitude of these signals was sampled at an interval of 0.8 ns for a total of 125 ns, resulting in 156 channels. Data processing tools were developed using `Julia` to first interpret the pulse information from these binary files and create HDF5 files for post-processing. A `Python` post-processing program was then used to obtain the final experimental neutron time-of-flight histograms for comparison with radiation transport simulations.

4.1.1. Pulse shape discrimination

Organic liquid scintillator detectors, such as EJ-301, are typically sensitive to both incident neutron and photon radiation. Meaning that each source of radiation can produce scintillation light, which after amplification by a PMT, results in an electrical signal which is transformed into digital pulse. Pulse shape discrimination (PSD) refers to separating these digital pulses by the differences in typical neutron and photon pulse shapes from the different reaction kinematics of each with the scintillator (Marrone et al., 2002). Since the presence of both types of radiation in the measured signal is undesirable for neutron and photon only measurements, several methods for exploiting the differences between neutron and photon pulse shapes have been developed (Kaschuck and Esposito, 2005 and Lang et al., 2017). Previous measurements at RPI with EJ-301 detectors have employed the fall-time comparison method (Saglime, 2009), and the standard fit method, or pulse shape classification method (PSC) (Daskalakis, 2015). Fig. 5 shows the typical separation observed between neutron and photon pulses measured with the large EJ-301 detectors in the RPI high energy neutron scattering system. Note that the signal is dominated by low-integral (energy) pulses. Therefore, correct classification of these pulses as neutrons or photons is paramount to utilizing most of the measured data.

An adaption of the PSC, or standard fit method, was used to separate neutron and photon interactions in this analysis. A single reference pulse shape for photon interactions was developed, but multiple reference pulse shapes were developed for neutron interactions as a function of pulse integral (proportional to incident neutron energy). The reference photon pulse shape was developed using approximately 520,000 digitized pulses measured from a ^{22}Na source, and is in good agreement with those previously developed (Daskalakis, 2015). The reference neutron pulse shapes considered approximately 82,000 pulses collected during this carbon neutron scattering measurement at a scattering angle of 150 degrees. Pulses believed to be incident photons were discarded, and the remaining neutron pulses were grouped into large bins of pulse integral, where the pulse shapes were averaged. The magnitude-normalized reference neutron pulse shapes for each pulse integral group are shown in Fig. 6 along with the single reference neutron pulse shape developed previously by Daskalakis (2015).

The implementation of this PSD method in the `Julia` data processing and `Python` post-processing programs is as follows. First, the `Julia` data processing program inverts the negative pulse amplitudes. Then, the average pretrigger signal in the first 14 channels of a pulse, or baseline, is subtracted from all channels of the pulse. Characterizing parameters of each pulse are then determined, including the peak location and magnitude, total & tail pulse integral, centroid, χ_n^2, χ_g^2, multiplicity, etc. Here, the tail pulse integral is the integral of a pulse between channels 22 and 100 following the peak channel. Additionally, the χ_n^2 and χ_g^2 values represent reduced chi-squared goodness-of-fit values between a pulse, and the aforementioned reference photon and appropriate reference neutron pulse shapes, respectively. A pulse is identified as a neutron or photon pulse by the lesser of these two quantities in the `Python` post-processing program. A gamma misclassification correction (GMC) function was also developed for this analysis to remove photon pulses which were falsely classified as neutrons, following the same methodology developed by Daskalakis (2015). The GMC remained below 2% under 5 MeV, and reached a maximum of about 4% above 5 MeV, which is consistent with previous experiments (Daskalakis et al., 2014). Note that truncated pulses were discarded. Pileup events, or other erroneous pulses, were also removed by filtering pulses by centroid and applying an upper-level discriminator in the PSD parameter space.

4.2. Neutron time-of-flight measurements

A quasi-differential neutron scattering measurement campaign at RPI typically includes multiple neutron time-of-flight measurements. These being measurements of:

1. The incident neutron flux profile on the scattering sample.

[3] MCNP® and Monte Carlo N-Particle® are registered trademarks owned by Triad National Security, LLC, manager and operator of Los Alamos National Laboratory (LANL). Any third party use of such registered marks should be properly attributed to Triad National Security, LLC, including the use of the designation as appropriate. For the purposes of visual clarity, the registered trademark symbol is assumed for all references to MCNP within the remainder of this paper.

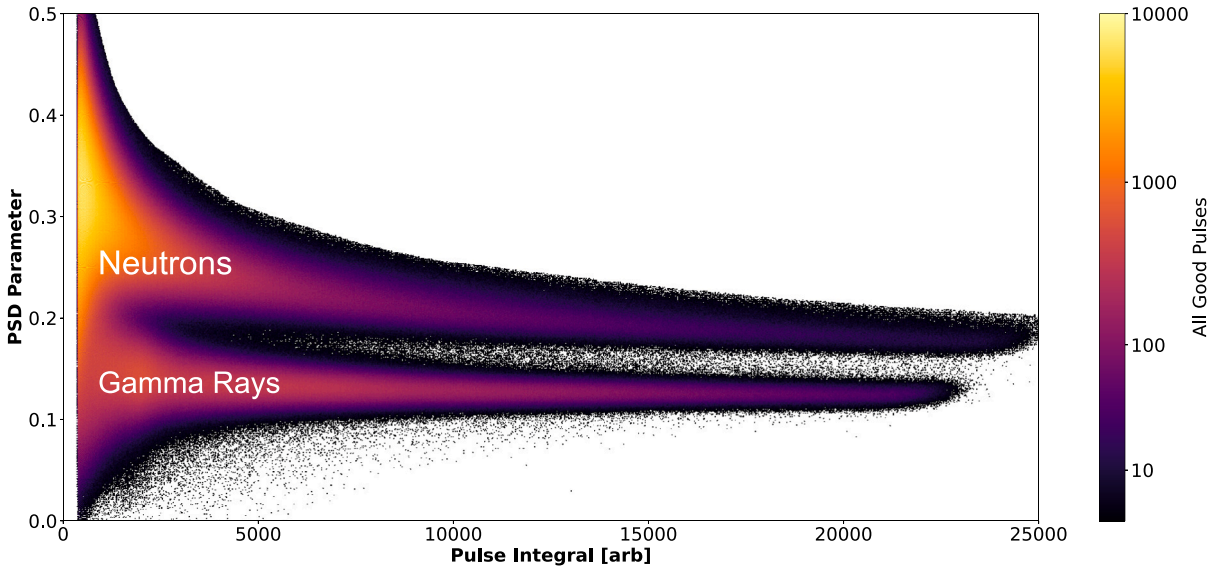

Fig. 5. Pulse shape discrimination histogram from pulses collected during the tantalum neutron scattering measurement. The PSD parameter is the ratio of the integral of the tail of a pulse (see Fig. 6) to its total integral, as a function of pulse integral (proportional to incident radiation energy).

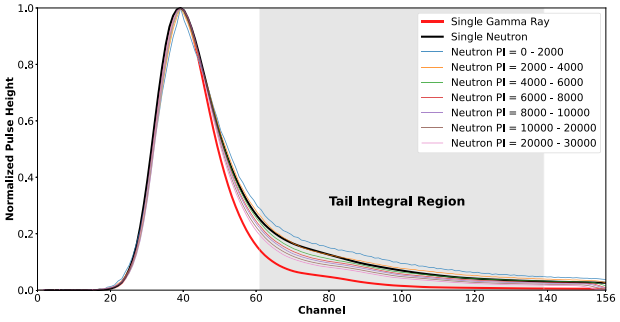

Fig. 6. Reference neutron and photon pulse shapes developed for the large EJ-301 scintillation detectors used in the RPI high energy neutron scattering system.

2. The relative neutron detection efficiency of each EJ-301 neutron detector.
3. Neutron scattering from the reference material, sample of interest, and open beam.

Quantities such as the incident neutron flux profile and relative neutron detection efficiencies can be modeled using codes such as MCNP6 and SCINFUL (Dickens, 1988). However, it is preferred to obtain these quantities experimentally. For this work, a neutron flux profile from previous measurements was adopted (Section 4.2.1), and the relative neutron detection profile of each EJ-301 detector was measured relative to the measured flux (Section 4.2.1). Table 1 summarizes the experimental conditions for all the neutron time-of-flight measurements performed in this work. An additional neutron transmission measurement was performed on a 2 cm right circular cylinder of Be to verify the neutron flight path length by observing the location of the 622 keV, 812 keV and 2.72 MeV resonances. For each measurement in Table 1, the data were collected in cycles of short LINAC trigger intervals to minimize potential data abnormalities due to fluctuations in LINAC beam conditions. To assess if a particular run cycle contained these anomalies, the ratio between the beam-monitor neutron counts and the neutron counts of each EJ-301 detector channel was compared to ensure correlation for all cycles throughout each measurement. Cycles possessing ratios beyond 3σ of the resultant distribution were removed, alongside problematic cycles noted in the run logs.

Table 1
Experimental conditions and total run time for neutron time-of-flight measurements performed. l_2 represents the flight path length from the center of the sample to the front face of an EJ-301 detector. These values are listed in Table 3.

Measurement	Flight path [m]	Tirggers per cycle	Total run time [h]
Tantalum scattering	30.070 ± 0.005 + l_2	388 000	39.0
Carbon scattering	30.070 ± 0.005 + l_2	205 000	20.6
Open scattering	30.070 ± 0.005 + l_2	150 000	15.0
EJ-301 efficiencies	30.115 ± 0.005	360 000	32.0
Beryllium	30.115 ± 0.005	360 000	4.0

All conversions between measured neutron time-of-flight and incident neutron energy were performed using,

$$E(t) = m_0c^2\left[\frac{1}{\sqrt{\left(1-\frac{\left(\frac{l}{t-t_0}\right)^2}{c^2}\right)}}-1\right] \tag{2}$$

where

$E(t)$ = kinetic energy corresponding to a measured neutron time-of-flight, t
m_0c^2 = rest mass energy of a neutron
l = flight path length (includes l_2 from Table 1 for scattering measurements)
t = measured neutron time-of-flight
t_0 = gamma flash arrival time (corrected for gamma-ray time-of-flight)
c = speed of light in vacuum

Eq. (2) accounts for relativistic effects, which become important when the neutron energy exceeds ~2 MeV. Note that Eq. (2) does not include energy lost due to collisions within the scattering sample. The neutron detection time, t, is measured relative to the LINAC pulse time. The time at which the intense burst of bremsstrahlung photons, or the gamma flash, arrives at the EJ-301 detectors from the neutron-producing target is also measured. The measured gamma flash time, however, does not correspond to the true generation time of the neutrons. The true neutron generation time, t_0, is calculated

by subtracting the experimentally measured gamma flash time by the calculated time-of-flight of the photons from the neutron-producing target to the detector. The gamma flash for the measurements presented in this work was measured to be 894 ns ± 2 ns, which corresponds to a t_0 of 794 ns ± 2 ns. All neutron time-of-flight measurements were also corrected for deadtime, which was calculated to be 160 ns for the SIS-3305 system using methods developed by McDermott (2016). The correction was implemented using a non-paralyzable deadtime correction algorithm developed at RPI; the impact of which was largest for the EJ-301 detector efficiency measurements, but did not exceed 10%.

4.2.1. Incident neutron flux measurement

The profile of the neutron flux incident on a sample in the RPI high energy neutron scattering system from the bare-bounce target has been well characterized. Saglime (2009) first measured the neutron flux profile using a ^{6}Li glass detector and the EJ-301 detectors, and Daskalakis et al. (2014) confirmed this measurement with another measurement using a ^{235}U fission chamber. The latter of which is adopted for this work. Thus, the neutron flux profile used is relative to the well-known ^{235}U fission cross section, and is displayed in Fig. 7. Note that this flux shape was corrected for neutron transmission through materials present in the neutron beam during the experiment. No significant alterations were made to this neutron beamline since the measurement of Daskalakis et al. (2014). Therefore, the neutron flux profile is assumed to remain consistent.

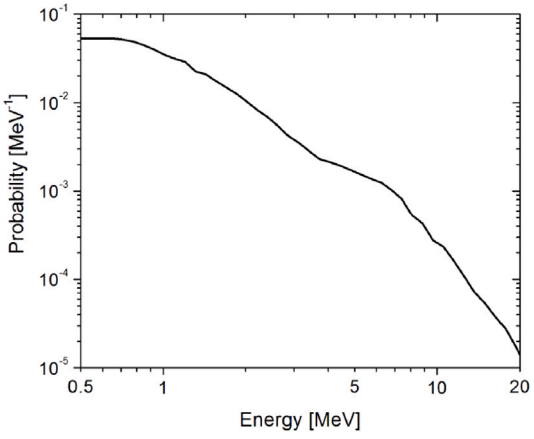

Fig. 7. The incident neutron flux profile, $\phi(E)$ from the bare-bounce target measured with a ^{235}U fission chamber below 1 MeV, and EJ-301 organic liquid scintillator detectors to 20 MeV as provided to MCNP for radiation transport simulations.
Source: Figure reproduced from Daskalakis (2015) with permission.

4.2.2. EJ-301 detector efficiency measurements

The relative neutron detection efficiency profile of each EJ-301 detector was derived using neutron time-of-flight spectroscopy. The responses of each detector to the known incident neutron flux profile were measured at a flight path length of 30.115 meters ± 0.005 meters by placing each EJ-301 detector in the center of the neutron beam. To perform these measurements without saturating the detectors, the RPI LINAC electron beam current was reduced to ~0.25 μA, and a second 0.984 inch ± 0.012 inch DU filter was added to the neutron beam. All measurements were normalized by neutron beam monitor counts, M_j, to the detector 1 efficiency measurement, M_1 (arbitrarily chosen). The measured responses were then compared to the known incident neutron flux shape, $\phi(E)$, from Section 4.2.1 using `MCNP6.3`. The relative neutron detection efficiency profile for each detector, η_j, was calculated using,

$$\eta_j(E_i) = \frac{(C_j(E_i) - G_j(E_i)) - B_0}{\phi(E_i)} \cdot \frac{M_j}{M_1} \tag{3}$$

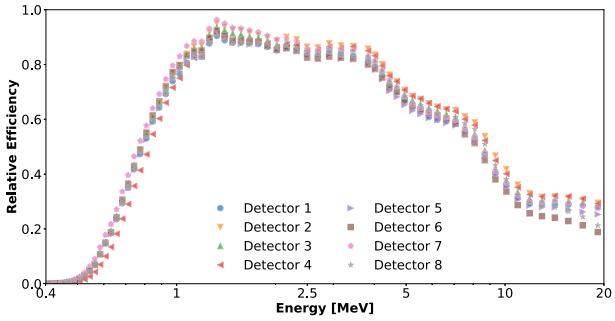

Fig. 8. Calculated relative neutron detection efficiencies for each of the eight EJ-301 detectors in the RPI high energy neutron scattering system.

The constant room neutron background, B_0, was obtained from long counts of the ambient room conditions. The photon room background signal was removed using PSD (Section 4.1.1). Photons falsely classified as neutrons, $G_j(E_i)$, were removed from the measured neutron counts for each EJ-301 detector, $C_j(E_i)$. After monitor normalization, good agreement was observed between the responses of all eight EJ-301 detectors, but slight differences were observed at low incident neutron energies. To most accurately model the behavior of the system these differences were retained, yielding eight unique neutron detection efficiency profiles. However, during initial testing a systematic overprediction of the measured carbon reference and open beam measurements at low incident neutron energies (high time-of-flight) was observed. To resolve this discrepancy, the lower level discriminator (LLD) of the measured in-beam efficiency data were increased, by ~11% on average, in post-proccessing. Thus decreasing the neutron detection efficiencies to best reproduce the measured neutron scattering spectra in the open beam and carbon reference experiments. The authors attribute this discrepancy to differences in experimental conditions between the in-beam efficiency and neutron scattering measurements. The final relative neutron detection efficiency profiles of the eight EJ-301 detectors in the RPI high-energy neutron scattering system used in all radiation transport simulations for this work are shown in Fig. 8. Note that these efficiencies have undergone a smoothing routine using a (Savitzky and Golay, 1964) algorithm to preserve the integrals of the measured neutron time-of-flight spectra. Good agreement is observed when using these efficiency profiles to reproduce the in-beam efficiency measurements (Fig. 9). Note that only statistical uncertainty is included with the experimental data.

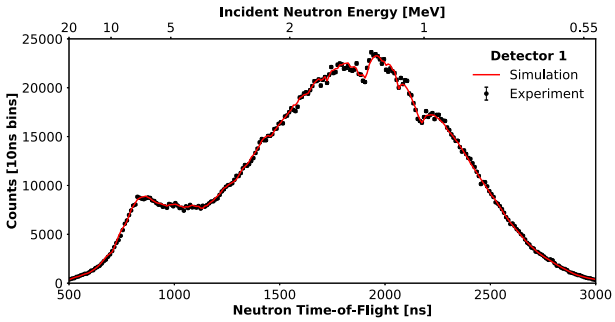

Fig. 9. Measured neutron flux using EJ-301 detector 1 compared to radiation transport simulation of the incident neutron flux considering the calculated relative neutron detection efficiency profile for EJ-301 detector 1.

4.2.3. Quasi-differential neutron scattering measurements

The final experimental components of a quasi-differential measurement campaign are the neutron scattering measurements of the sample of interest, the reference material, and the open beam. For this experiment, neutron scattering was measured from right cylindrical

samples of elemental carbon (reference material) and 99.95% pure tantalum. The LINAC beam parameters during these measurements were provided in Section 3.1. The neutron time-of-flight histograms, $C_{i,j}$, for the tantalum and carbon scattering measurements were obtained by removing both the monitor-normalized open-beam (background) contribution and photons which were falsely classified as neutrons using,

$$C_{i,j} = (C^S_{i,j} - G^S_{i,j}) - (C^O_{i,j} - G^O_{i,j}) \cdot \left(\frac{M_S}{M_O}\right) \tag{4}$$

where

$C^S_{i,j}$ = counts in time-of-flight bin i for EJ-301 detector j during sample in measurement
$G^S_{i,j}$ = gamma misclassification counts in time-of-flight bin i for EJ-301 detector j during sample in measurement
$C^O_{i,j}$ = counts in time-of-flight bin i for EJ-301 detector j during open beam measurement
$G^O_{i,j}$ = gamma misclassification counts in time-of-flight bin i for EJ-301 detector j during open beam measurement
M_S = sum of monitor counts in time-of-flight region of interest recorded during a sample in measurement
M_O = sum of monitor counts in time-of-flight region of interest recorded during an open beam measurement

The uncertainty corresponding to the neutron counts measured in each time-of-flight bin, for each neutron detector $\Delta C_{i,j}$, is the quadrature sum of the statistical and systematic uncertainties was determined using,

$$\Delta C_{i,j} = \sqrt{\left(\sigma^{stat}_{i,j}\right)^2 + \left(\sigma^{sys}_{i,j}\right)^2} \tag{5}$$

In Eq. (5), the statistical uncertainty of the neutron counts, $\sigma^{stat}_{i,j}$, was obtained through standard error propagation for uncorrelated variables, Knoll (2010),

$$\sigma^{stat}_{i,j} = \left(C^S_{i,j} + G^S_{i,j} + C^O_{i,j} \cdot \left(\frac{M_S}{M_O}\right)^2 + G^O_{i,j} \cdot \left(\frac{M_S}{M_O}\right)^2 + M^S \cdot \left(\frac{C^O_{i,j} - G^O_{i,j}}{M_O}\right)^2 + \left(C^O_{i,j} - G^O_{i,j}\right)^2 \cdot \left(\frac{M_S^2}{M_O^3}\right)\right)^{\frac{1}{2}} \tag{6}$$

The systematic uncertainty, $\sigma^{sys}_{i,j}$, is the ratio between the standard deviation of the area normalization factors between the measured and simulated carbon reference neutron time-of-flight histograms, provided in Fig. 13 as ϵ_{sys}, and the mean value. $\sigma^{sys}_{i,j}$ represents the total systematic uncertainty present in the measurement from all sources, and was obtained using,

$$\sigma^{sys}_{i,j} = C_{i,j} \cdot \frac{\sqrt{\frac{\sum_j (N_j - \mu)^2}{N^D - 1}}}{\mu} \tag{7}$$

where

N_j = the area normalization factor between the carbon reference measurement and corresponding MCNP simulation for detector j
μ = the average area normalization factor between the carbon reference measurement and corresponding MCNP simulation across all scattering angles
N^D = number of detectors

Additional details regarding the systematic uncertainty calculation are presented in Section 5.2.1.

The dimensions of the samples used in this experiment were characterized using calibrated measurement devices, and mass spectroscopy was used to quantify sample contamination. Table 2 lists the measured characteristics of both samples. The detectable impurities present in the beryllium, carbon, and tantalum samples were negligible in these measurements, and are given in Rapp (2011). The carbon sample was also baked at 150 C for 24 hours to remove any absorbed water. The positions of the eight EJ-301 detectors relative to the center of the scattering sample for the neutron scattering measurements are listed in Table 3. The uncertainties listed correspond to a reproducibility study of the positional measurement techniques. Energy calibration was performed using an ^{22}Na gamma-ray source and a mixed neutron and gamma-ray source of PuBe shielded with HDPE (to use the 2.2 MeV hydrogen de-excitation gamma-ray). Regular calibration checks were performed throughout the experiment using ^{137}Cs and ^{60}Co sources, and minor voltage tweaks (< 3 V) were applied appropriately. The calibration was then verified at the conclusion of the experiment. No large drifts in the PMT gain were observed. The LLD was set to 10 bits on all detector channels.

Table 2
Measured sample characteristics.

Sample	Thickness [cm]	Diameter [cm]	Mass [g]	Calculated density [g/cc]
Carbon	7.003 ± 0.002	7.495 ± 0.002	521.8 ± 0.1	1.689 ± 0.001
Tantalum	5.535 ± 0.002	7.626 ± 0.002	4218.7 ± 0.1	16.67 ± 0.01
Beryllium	2.000 ± 0.002	7.498 ± 0.002	163.08 ± 0.01	1.847 ± 0.002

Table 3
EJ-301 detector positions.

#	Theta [Degrees]	Phi [Degrees]	Distance [cm]
1	45 ± 1.25	133.5 ± 2	54.3 ± 0.2
2	30 ± 1.25	34.3 ± 2	54.1 ± 0.2
3	60 ± 1.25	122.5 ± 2	52.5 ± 0.2
4	95 ± 1.25	54.5 ± 2	54.6 ± 0.2
5	125 ± 1.25	136.5 ± 2	54.0 ± 0.2
6	110 ± 1.25	57.5 ± 2	47.6 ± 0.2
7	150 ± 1.25	25.5 ± 2	50.4 ± 0.2
8	150 ± 1.25	129.7 ± 2	56.0 ± 0.2

4.3. MCNP6.3 radiation transport simulations

Radiation transport simulations using `MCNP6.3` were used to compare the performance of evaluated nuclear datasets with the experimentally measured neutron scattering spectra. Assessing evaluated nuclear data in this manor is acceptable since the following system variables have been well studied, characterized, and/or validated:

1. The experimental apparatus and geometry (Fig. 10)
2. The incident neutron flux shape, and parameters of the RPI LINAC (Section 4.2.1)
3. The relative neutron detection efficiency of the EJ-301 detectors (Section 4.2.2)
4. Monte-Carlo radiation transport techniques

The lone variable remaining in the system which greatly influences the simulated neutron scattering spectrum is the evaluated nuclear data used. For all simulations performed of neutron scattering, the `F5` point-detector tallying method was used with ENDF/B-VIII.0 nuclear data for all materials, except for ^{181}Ta which was varied. To directly compare the MCNP simulation to the experimental data, a normalization factor must be applied to the simulation since the absolute neutron flux is unknown. This normalization corresponds to the ratio between the integral of the background-subtracted neutron time-of-flight histogram of the carbon experiment to that of the MCNP simulation within equal neutron time-of-flight bounds.

For this experiment, improvements were made to the geometry present within the model to further reduce the uncertainty associated with the comparison of the simulation with the experiment, the new model is shown in Fig. 10. The summation of the following components influenced the average integral of the full simulated detector response of the open beam at all angles by approximately 3.2% which had not previously been studied:

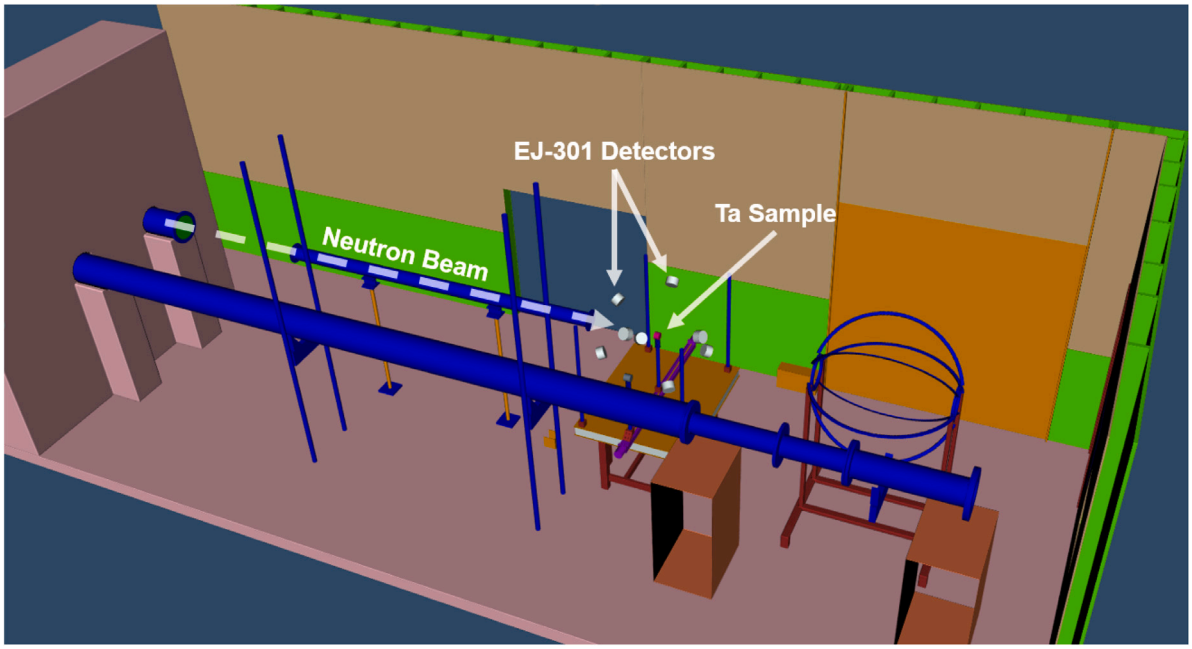

Fig. 10. Detailed model geometry present in MCNP for simulating the detector responses during a high energy neutron scattering measurement.

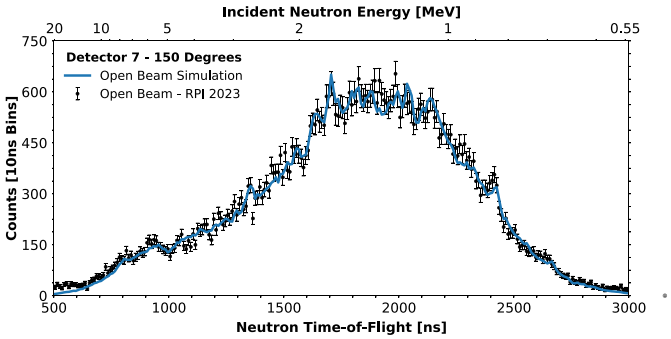

Fig. 11. Area-normalized open beam experiment simulated with MCNP shows good agreement compared to the measured data.

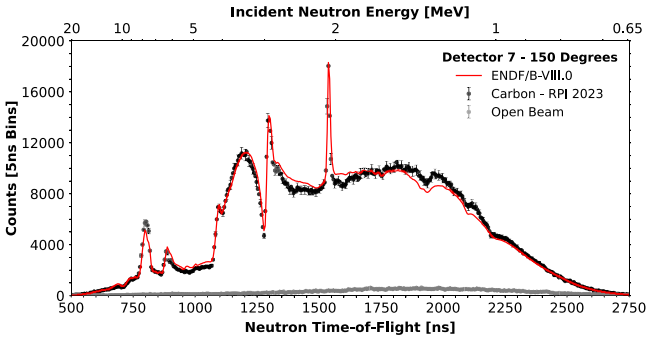

Fig. 12. Carbon neutron scattering time-of-flight histogram including the small, monitor-normalized, open beam background contribution.

- The 3-foot concrete shielding wall between the LINAC "tunnel" and the 25 m flight station
- The walls of the 25 m station (including an aluminum plate on the wall behind the high energy scattering system in the neutron beam)
- The collimation present in the RPI LINAC West neutron beam line

5. Experimental results and discussion

Results from the neutron scattering measurements of the tantalum and carbon samples are presented in this section. Validation of the experimental geometry model, which reproduces the LINAC-induced neutron background and room return, is also shown. Monte-Carlo uncertainties on all figures in this section are omitted since these errors fall within the width of the lines plotted.

5.1. Open beam characterization

To validate the model shown in Fig. 10, radiation transport simulations of the open beam measurement, or LINAC-induced neutron background, were performed. The signal measured during an open beam run is dominated by neutron scattering from air and room return. Therefore, accurately modeling the experimental geometry is required to correctly reproduce the open-beam experiment. Fig. 11 shows an example of these results, and Fig. 12 shows the contribution of the open beam to a carbon scattering measurement. Generally good agreement is observed between the open beam simulation and the experiment at all detector angles.

5.2. Carbon neutron scattering measurement

The neutron scattering measurement from the reference material is utilized in several aspects of the quasi-differential scattering method. As discussed in Section 4, the results from the neutron scattering measurement of the reference material are used to verify the experimental method and simulation geometry, determine a normalization between simulation and experiment, and estimate the systemic uncertainty of the experiment. Comparisons of the background-subtracted measured carbon neutron scattering spectrum and the area-normalized background-subtracted simulated carbon neutron scattering spectra are presented in Fig. 14. Overall, good agreement is observed between the measured carbon neutron scattering and the ENDF/B-VIII.0 evaluation

in the incident neutron energy range of 0.65 MeV to 20 MeV at all scattering angles measured.

Some discrepancies between the measured carbon neutron scattering data and the ENDF/B-VIII.0 evaluation were observed. These include an overprediction of carbon neutron scattering at between 4 MeV to 8 MeV, and an underprediction of carbon neutron scattering at between 1 MeV to 1.5 MeV, both predominantly at very backward scattering angles. The former is attributed to potential issues in the neutron detection efficiency profiles. And the latter discrepancy was previously observed in measurements by Saglime (2009) and Daskalakis (2015). Ultimately, these discrepancies were not deemed harmful to the validation of this experiment, and can be used to improve the evaluated carbon datasets.

5.2.1. Systematic uncertainty quantification

The average deviation of this carbon neutron scattering measurement from the ENDF/B-VIII.0 elemental carbon data was adopted as the systematic uncertainty of these quasi-differential neutron scattering measurements. These measurements therefore treat the ENDF/B-VIII.0 elemental carbon nuclear data as a reference since these data are well known. This deviation encompasses all potential sources of uncertainty in the quasi-differential methodology such as those present in the neutron flux shape and neutron detection efficiency profiles. The systematic uncertainty was obtained using Eq. (5), which describes the average deviation in area normalization factors between the carbon neutron scattering simulation and the experiment of all measured scattering angles. The area normalization factors were determined using the integration region of 500 ns to 2750 ns, or 20 MeV to 0.65 MeV, and the systematic uncertainty of this neutron scattering experiment was calculated to be 4.0%. The deviations of each scattering angle (detector) with respect to the mean are presented in Fig. 13. In previous elemental carbon quasi-differential neutron scattering measurements at RPI, it was typical to observe normalization outliers and/or average deviations in excess of 6% (Daskalakis, 2015, Blain et al., 2022). The reduction in systematic uncertainty in this experiment is justified by reducing the uncertainty of the sample position throughout the experiment, developing a more accurate model for radiation transport simulations, and the implementation of a more rigorous detector alignment procedure.

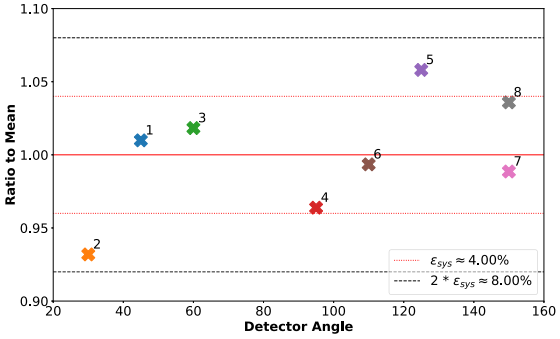

Fig. 13. Deviation of area normalization factors between the elemental carbon quasi-differential neutron scattering measurement and simulation using ENDF/B-VIII.0 at all measured scattering angles. Annotations denote arbitrary detector numbers.

5.3. Tantalum neutron scattering measurement

In the previous section, the carbon neutron scattering measurement was demonstrated to accurately reproduce the ENDF/B-VIII.0 elemental carbon evaluation. Since good agreement was observed, the measured tantalum neutron scattering data can be used to assess the performance of evaluated ^{181}Ta datasets. To properly compare the tantalum neutron scattering data to simulation, the detector area normalization factors from the carbon analysis are used, but are scaled by the ratio of total monitor counts (proportional to LINAC run time) between the tantalum and carbon measurements. Fig. 15 shows the results between the background-subtracted measured tantalum neutron scattering spectrum and the area-normalized background-subtracted tantalum neutron scattering simulation. Note that Ta neutron scattering data is reported to 3000 ns, or 0.55 MeV, which is beyond the validation region of the elemental carbon measurement due to the lower lethargy gain per collision of Ta. Since both the neutron flux shape and detector efficiency profiles in this region are known, the data are provided. Additionally, forward neutron scattering angles refer to a measurement of neutron scattering where $\theta < 90$ degrees, or the cosine of the scattering angle, μ is positive. Likewise, backward neutron scattering angles refer those where $\theta \geq 90$ degrees or $\mu \leq 0$, relative to the incident neutron beam.

5.3.1. Forward neutron scattering angles

Tantalum neutron scattering measured at forward scattering angles showed mixed agreement with the various evaluated ^{181}Ta datasets. At 30 degrees (Fig. 15a), all ^{181}Ta evaluations generally underestimate the experimental data above 700 keV, except the ENDF/B-VIII.0, JEFF-3.3, and TENDL-2023u datasets between approximately 1 MeV and 2 MeV. However, the shape of the recent ENDF/B-VIII.1 and JENDL-5.0 ^{181}Ta evaluations visually appear to better represent the data despite a ~20% discrepancy in magnitude. This observation suggests that improvements in both the shape elastic and inelastic scattering components of these ^{181}Ta evaluations have been made, but adjustments are still needed.

Better agreement between the ENDF/B-VIII.1 ^{181}Ta evaluation and the measured Ta neutron scattering is observed consistently at both 45 degrees (not pictured) and 60 degrees (Fig. 15b). Here, the ENDF/B-VIII.1 dataset underpredicts the experiment in between 1 MeV and 2 MeV by up to ~15%, but agrees within experimental uncertainty for all remaining incident neutron energies. The JENDL-5.0 ^{181}Ta evaluation shows similar agreement to that of ENDF/B-VIII.1. The ENDF/B-VIII.0, JEFF-3.3, and TENDL-2023u datasets overestimate Ta neutron scattering between 1.5 MeV and 2.5 MeV. Seemingly, corrections made to the ENDF/B-VIII.1 ^{181}Ta evaluation overcompensated for the overprediction of neutron scattering present in the previous ENDF/B-VIII.0 evaluation. These results suggest that further improvements can be made to the double-differential scattering cross sections when $\mu > 0$.

5.3.2. Backward neutron scattering angles

A particular emphasis was placed on validating neutron scattering reactions with tantalum at backward scattering angles due to neutron reflection implications. Overall, good agreement is observed between all evaluated ^{181}Ta datasets and the experimental data above 5 MeV. However, profound discrepancies between theory and experiment were observed below this energy at all measured backward scattering angles. Specifically, the ENDF/B-VIII.0, JEFF-3.3, and TENDL-2023u evaluated ^{181}Ta datasets overestimate the measured Ta neutron scattering spectra up to ~70% between approximately 700 keV and 3 MeV at scattering angles of 95, 110, 125, and 150 degrees (Fig. 15(c)(d)(e)(f)). Fortunately, the ENDF/B-VIII.1 and JENDL-5.0 ^{181}Ta evaluations mostly resolved this region of disagreement by reducing both the elastic and inelastic scattering channels (Fig. 17). Smaller discrepancies, below 10%, remain however between the ENDF/B-VIII.1 and JENDL-5.0 ^{181}Ta datasets and the measured Ta neutron scattering data between 1 MeV and 2 MeV when $\mu \leq 0$.

5.3.3. Scattering Kernel balance

The improved performance of the ENDF/B-VIII.1 and JENDL-5.0 libraries at backward scattering angles is particularly encouraging from a criticality safety perspective. Since tantalum criticality safety concerns involve reflection of high energy fission neutrons (Hutchinson et al., 2024), accurately modeling neutron re-entry flux from reflection is paramount to designing and performing safe operations. The overall agreement between the ^{181}Ta evaluated nuclear datasets investigated

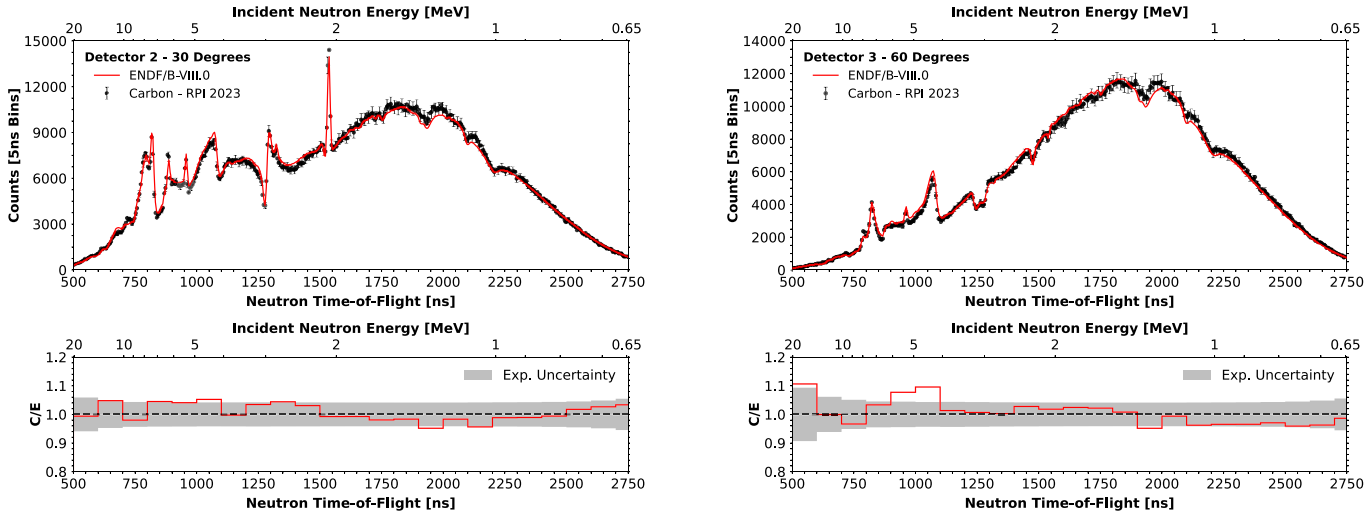

(a)

(b)

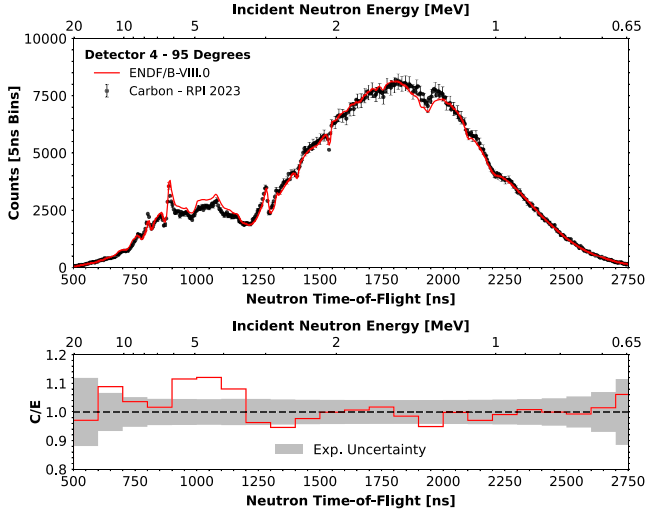

(c)

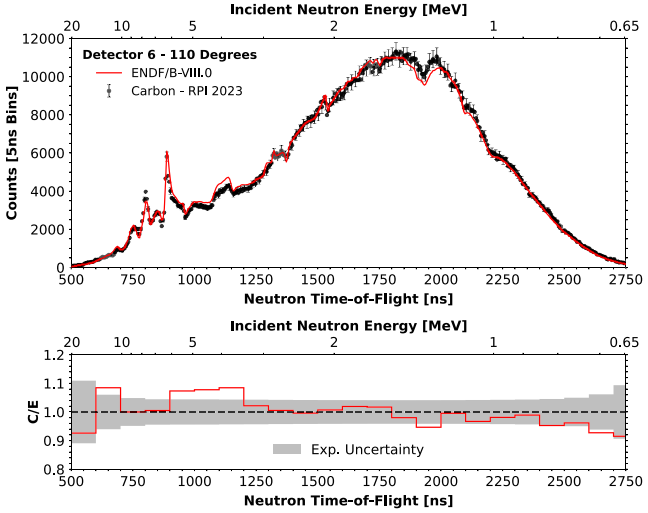

(d)

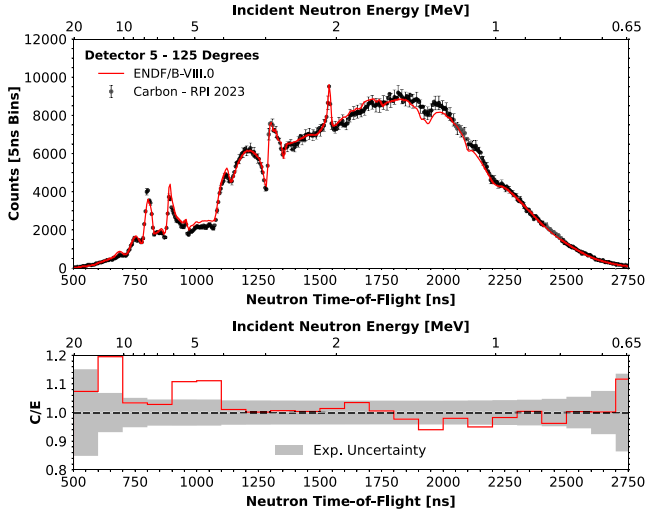

(e)

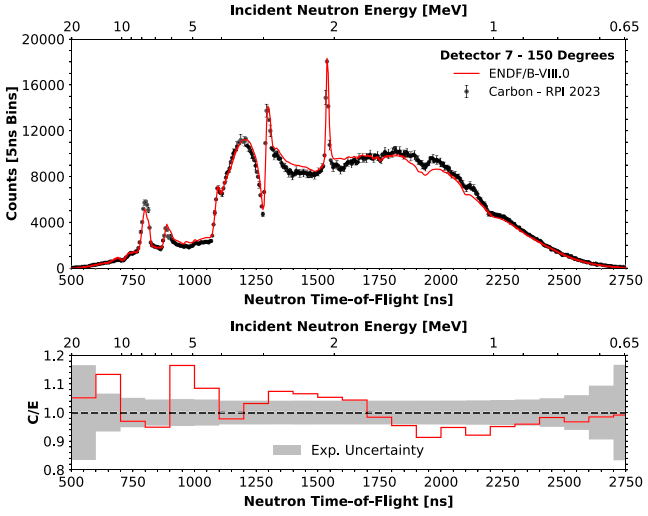

(f)

Fig. 14. (a,b,c,d,e,f) Experimentally measured carbon neutron scattering (E) as a function of neutron time-of-flight compared to MCNP radiation transport simulation (C) at forward and backward neutron scattering angles relative to the incident neutron beam. Ratios of simulation to experiment (C/E) are provided to highlight areas of agreement and disagreement.

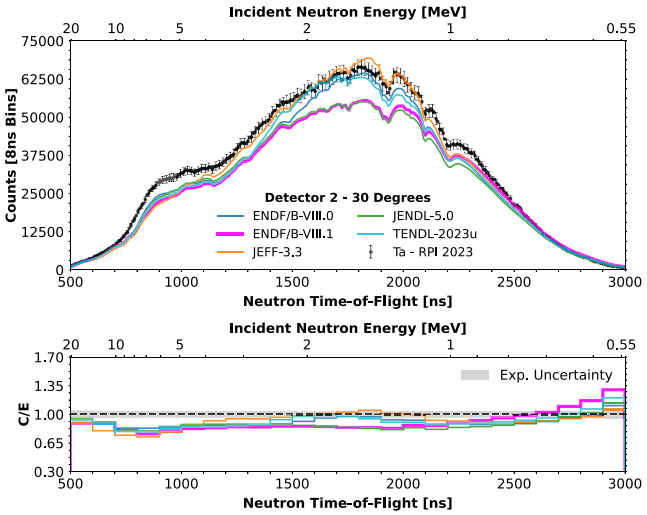

(a)

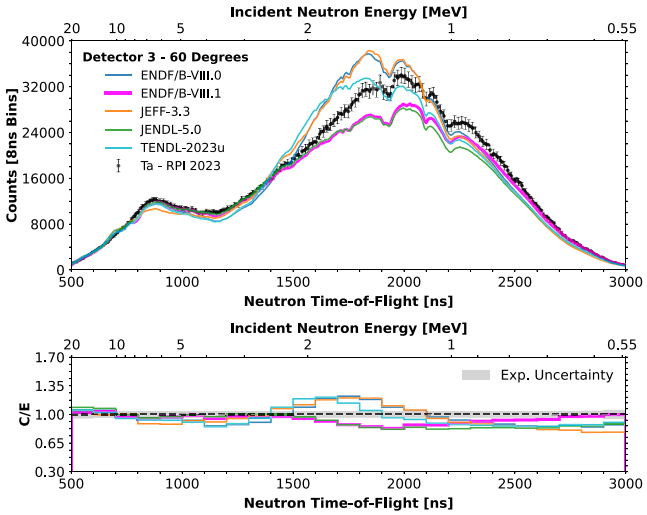

(b)

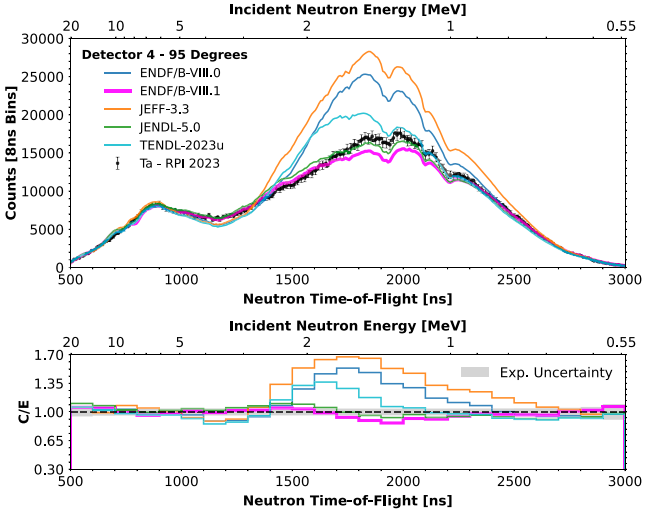

(c)

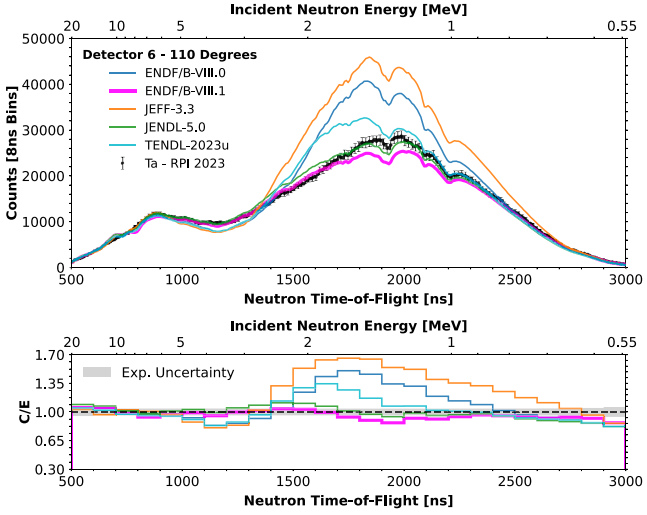

(d)

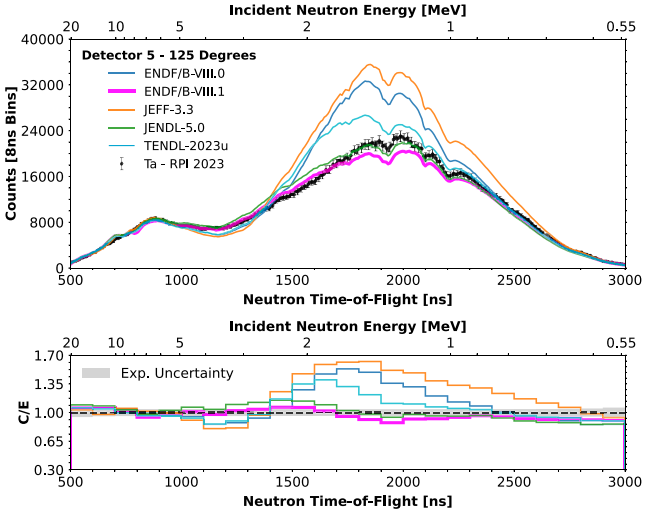

(e)

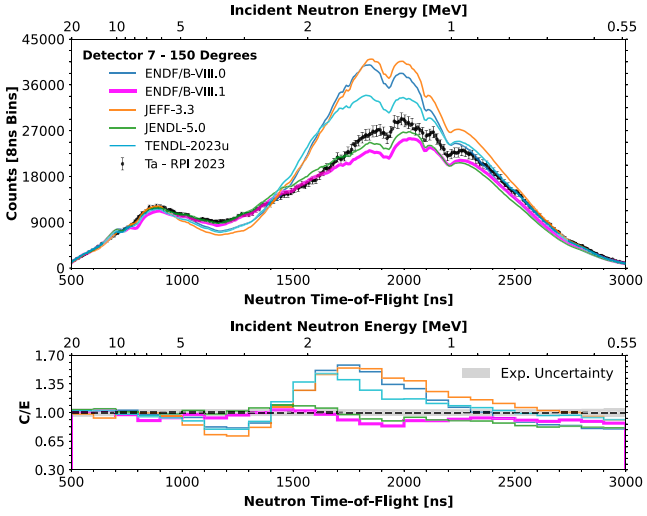

(f)

Fig. 15. (a,b,c,d,e,f) Experimentally measured tantalum neutron scattering (E) as a function of neutron time-of-flight compared to MCNP radiation transport simulation (C) at forward and backward neutron scattering angles relative to the incident neutron beam. Ratios of simulation to experiment (C/E) are provided to highlight areas of agreement and disagreement.

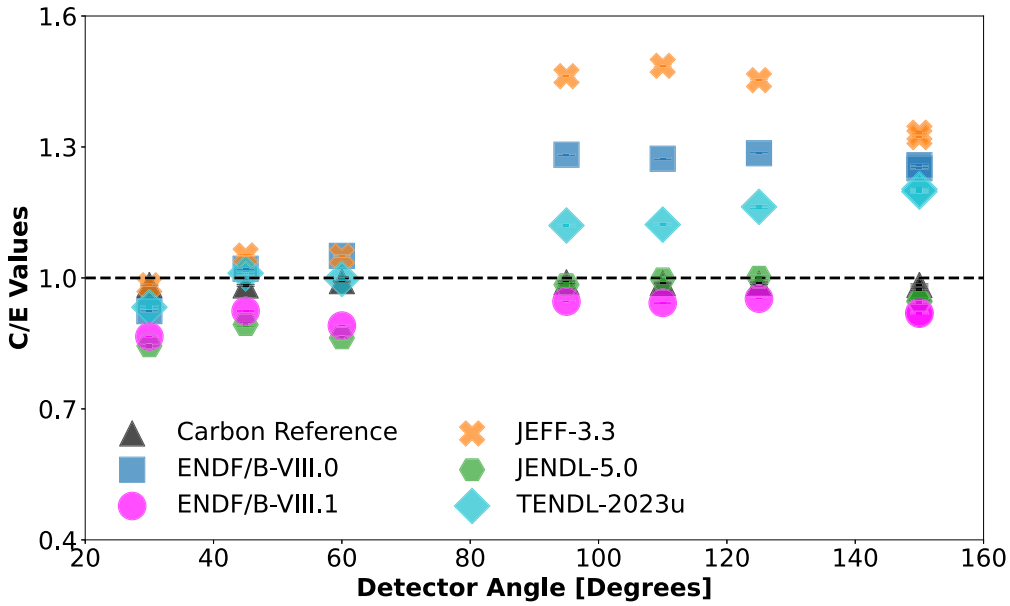

Fig. 16. Ratio of MCNP simulation (C) of total tantalum neutron scattering to the experimental data (E) for all detector angles measured between 0.75 MeV and 2.5 MeV.

and the experimental data between 0.75 MeV and 2.5 MeV is provided in Fig. 16. In which, the backward scattering bias present in the ENDF/B-VIII.0, JEFF-3.3, and TENDL-2023u ^{181}Ta evaluations is apparent. Moreover, the superior agreement between the ENDF/B-VIII.1 and JENDL-5.0 evaluated ^{181}Ta datasets and the experimental Ta neutron scattering data is illustrated. These experimental findings thus provide an independent validation of the ability of the ENDF/B-VIII.1 and JENDL-5.0 ^{181}Ta evaluated nuclear data to most accurately model the high energy neutron scattering behavior of Ta.

5.3.4. Reaction channel contributions

To further investigate the discrepancies observed between the Ta neutron scattering data and the ^{181}Ta evaluated nuclear datasets, radiation transport simulations isolating certain ^{181}Ta reaction channels were performed. Inelastic scattering, and all other neutron producing reactions of ^{181}Ta (besides elastic scattering), were isolated using the tally `tag` method. And the ^{181}Ta elastic scattering contribution was derived using both the tally `tag` method, and the cell identifying tally flag, `ICD`. Specifically, the sum of all non-elastic neutron producing channels (the `tagged` tallies) were subtracted from the total neutron emissions from the Ta sample cell (the `ICD` tally), yielding the elastically scattered neutrons from ^{181}Ta. Note that neutrons only score to both the `ICD` and `tag` tallies if the neutron collided with ^{181}Ta within the sample cell. Therefore, these simulations include limited secondary effects such as room return and sample impurities, the contributions of which though are small. Moreover, the small measured open-beam background contribution was not removed from these tallies since the contribution of which cannot be accurately distributed amongst reaction channels.

The results from these simulations at a scattering angle of 110 degrees are presented in Fig. 17. Here, *Inelastic* denotes the sum of all partial inelastic channels and the continuum, and *Other Neutron Emissions* denotes the sum of all other available neutron producing reactions in the ^{181}Ta dataset, such as (n,3n), (n,n2p), etc. The total simulation, labeled as the nuclear data library, corresponds to the results in Fig. 15. This investigation suggests the overestimation of the Ta scattering data by the ENDF/B-VIII.0 and TENDL-2023u ^{181}Ta datasets is driven by issues in both elastic and inelastic scattering. On the contrary, the elastic scattering channel dominates the JEFF-3.3 simulation leading to overprediction. This observation is consistent with the evaluated nuclear data shown in Fig. 1. Strong agreement is seen between both the elastic and inelastic scattering channels of the ENDF/B-VIII.1 and JENDL-5.0 ^{181}Ta evaluations. These trends are generally consistent at all measured scattering angles. The inconsistencies observed between the evaluated ^{181}Ta datasets below 5 MeV incident neutron energy suggest a lack of available experimental nuclear reaction data to properly constrain these reaction channels.

6. Conclusions

An experiment was conducted at the RPI linear accelerator center to measure neutron scattering from tantalum from 0.65 MeV to 20 MeV using neutron time-of-flight spectroscopy. The quasi-differential method was used to investigate the performance of the ENDF/B-VIII.0, ENDF/B-VIII.1, JEFF-3.3, JENDL-5.0, and TENDL-2023u ^{181}Ta incident neutron evaluations using `MCNP6.3`. This measurement provided an independent validation of the new ^{181}Ta high energy region incident neutron evaluation for the release of the ENDF/B-VIII.1 evaluated nuclear data library. Several upgrades were made to the physical RPI high energy neutron scattering system prior to this experiment which increased neutron detection efficiency above 3 MeV and decreased sample position uncertainty. These upgrades, alongside an enhanced radiation transport model, decreased the systematic uncertainty of experiment, allowing for more accurate comparisons with evaluated nuclear data.

Neutron scattering was measured from a reference sample of elemental carbon to validate the experimental findings. The measured neutron scattering from carbon reproduced the ENDF/B-VIII.0 carbon evaluations to 4.0% on average, which was adopted as the systematic uncertainty of the experiment. Overall, the new ENDF/B-VIII.1 high energy region ^{181}Ta evaluation was in good agreement with the experimental data, particularly above 2 MeV. Moreover, this evaluation mostly resolved the significant overestimation of backward ($\mu \leq 0$) neutron scattering present in the ENDF/B-VIII.0 ^{181}Ta evaluation. However, the ENDF/B-VIII.1 ^{181}Ta evaluation underestimates the measured Ta neutron scattering between 1 MeV and 2 MeV at all measured scattering angles. And, underestimates the entirety of the Ta neutron scattering data by about 20% at 30 degrees, despite better agreement between the shape of the scattering distribution and the experimental data.

Evaluated ^{181}Ta nuclear data from The ENDF/B-VIII.0, JEFF-3.3, and TENDL-2023u libraries significantly overestimate the measured Ta neutron scattering at backward scattering angles between 1 MeV and 3 MeV. The double-differential elastic and inelastic scattering cross

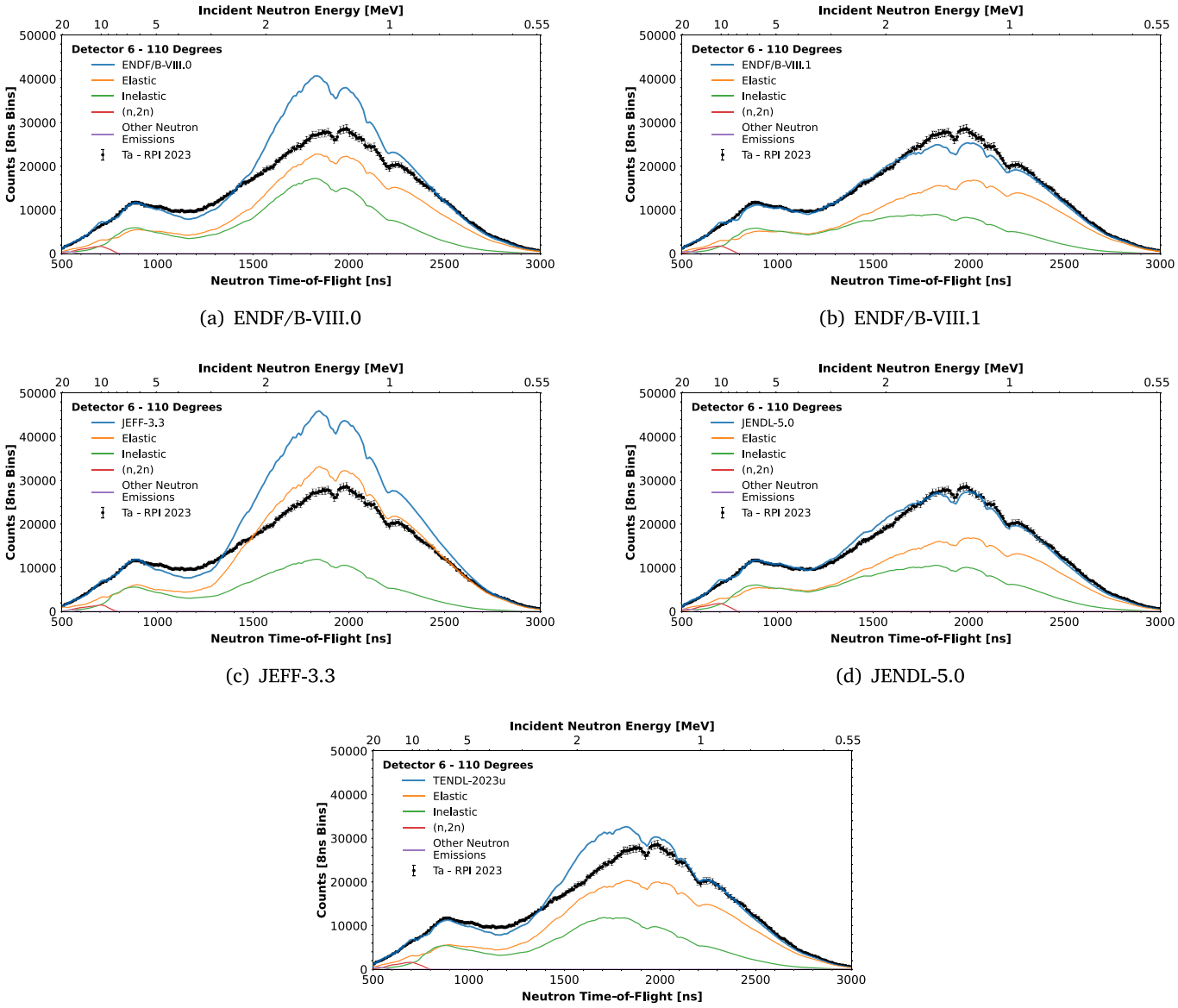

(a) ENDF/B-VIII.0

(b) ENDF/B-VIII.1

(c) JEFF-3.3

(d) JENDL-5.0

(e) TENDL-2023u

Fig. 17. (a,b,c,d,e) Experimentally measured tantalum neutron scattering compared to MCNP simulation for detector 6, placed at 110 degrees relative to the incident neutron beam. The tag and ICD treatments were applied to the F5 point detector tally to isolate neutron-emitting reaction channels using ENDF/B-VIII.0, ENDF/B-VIII.1, JEFF-3.3, JENDL-5.0, and TENDL-2023u ^{181}Ta nuclear data.

sections in these evaluations were observed to vary greatly, suggesting that few constraints were available on these reaction channels during evaluation. The JENDL-5.0 ^{181}Ta evaluation reproduced the experiment well, similarly to the ENDF/B-VIII.1 evaluation. The findings in this work support using either the ENDF/B-VIII.1 or the JENDL-5.0 ^{181}Ta evaluations for neutron transport simulations involving the material above 0.55 MeV incident neutron energy.

7. Future studies

The authors recommend further developing existing capabilities at RPI to accurately separate elastic and inelastic scattering interactions with nuclei with high level densities such as tantalum experimentally. And, to perform new measurements of tantalum elastic and inelastic scattering to support future ^{181}Ta evaluation efforts. Furthermore, performing a benchmark-level analysis (or uncertainty quantification) on this experiment, for inclusion in the international criticality safety benchmark evaluation project handbook (ICSBEP), for example, would provide a more robust validation platform for future nuclear data evaluations and criticality safety applications.

CRediT authorship contribution statement

Gregory J. Siemers: Conceptualization, Investigation, Methodology, Software, Data curation, Validation, Visualization, Formal analysis, Writing – original draft. **Yaron Danon:** Conceptualization, Investigation, Methodology, Software, Project administration, Funding acquisition, Supervision, Writing – review & editing. **Sukhjinder Singh:** Investigation, Software, Resources. **Katelyn C. Keparutis:** Investigation, Resources. **Peter J. Brain:** Investigation, Resources. **Benjamin H. Wang:** Investigation, Resources. **Adam M. Daskalakis:** Software, Resources. **Devin P. Barry:** Writing – review & editing, Resources. **Michael J. Rapp:** Resources. **Robert C. Block:** Resources.

Declaration of competing interest

The authors declare that they have no known competing financial interests or personal relationships that could have appeared to influence the work reported in this paper.

Acknowledgments

The authors first thank the RPI LINAC technical staff. Without the expertise from these individuals, this experiment could not have been performed: Peter Brand, Matthew Gray, Edwin Frank, Brian Martindale, Azeddine Kerdoun, Michael Bretti, and John Fava. The experimental portion of this work was funded by the Nuclear Criticality Safety Program, funded and managed by the National Nuclear Security Administration for the U.S. Department of Energy. The first author was supported in part by both the United States Nuclear Regulatory Commission (grant NRC-HQ-60-17-G-0006), and the United States National Nuclear Security Administration office of Naval Reactors' Naval Nuclear Propulsion Program.

Data availability

Data will be made available on request.

References

Barry, D.P., et al., 2013. Quasi-differential neutron scattering in zirconium from 0.5 to 20 MeV. Nucl. Sci. Eng. 172 (2), 188–201. http://dx.doi.org/10.13182/NSE12-1.

Barry, D.P., et al., 2024. A new ta-181 neutron Resolved Resonance Region evaluation. Ann. Nucl. Energy 208, 110778. http://dx.doi.org/10.1016/j.anucene.2024.110778.

Blain, E., et al., 2022. Measurements of neutron scattering from a copper sample using a quasi-differential method in the region from 2 keV to 20 MeV. Nucl. Sci. Eng. 196 (2), 121–132. http://dx.doi.org/10.1080/00295639.2021.1961542.

Brain, P., 2023. Neutron Evaluation and Validation of Natural Lead Isotopes for Fast Spectrum Systems (Ph.D. thesis). Rensselaer Polytechnic Institute.

Brown, D., Chadwick, M., Capote, R., et al., 2018. ENDF/B-VIII.0: the 8^{th} major release of the nuclear reaction data library with CIELO-project cross sections, new standards and thermal scattering data. Nucl. Data Sheets 148, 1–142. http://dx.doi.org/10.1016/j.nds.2018.02.001, Special Issue on Nuclear Reaction Data.

Brown, J.M., et al., 2019. Validation of unresolved neutron resonance parameters using a thick-sample transmission measurement. Nucl. Sci. Eng. 194 (3), 221–231. http://dx.doi.org/10.1080/00295639.2019.1688087.

Brown, J.M., et al., 2023. New measurements to resolve discrepancies in evaluated model parameters of ^{181}ta. Nucl. Sci. Eng. 1–11. http://dx.doi.org/10.1080/00295639.2023.2249786.

Brown, J.M., et al., 2025. Unresolved resonance parameter evaluation and uncertainty quantification of n+181ta reactions. Ann. Nucl. Energy 212, 111013. http://dx.doi.org/10.1016/j.anucene.2024.111013.

CAEN, 2005. Technical information manual - MOD. A 1733 - A 1833 -A 1733B - A 1833B 12/28 Channel HV boards manual Rev7. URL: https://groups.nscl.msu.edu/nscl_library/manuals/caen/MOD.A1733B-A1833B.pdf.

Capote, R., et al., 2014. Physics of neutron interactions with ^{238}U: New developments and challenges. Nucl. Data Sheets 118, 26–31. http://dx.doi.org/10.1016/j.nds.2014.04.003.

Daskalakis, A.M., 2015. Measurement of Elastic and Inelastic Neutron Scattering in the Energy Range from 0.5 to 20 MeV (Ph.D. thesis). Rensselaer Polytechnic Institute.

Daskalakis, A.M., 2023. Examining beryllium scattering using RPI quasi-differential Measurements and ENDF evaluations. https://indico.bnl.gov/event/18701/contributions/82624/.

Daskalakis, A., et al., 2014. Quasi-differential neutron scattering from ^{238}U from 0.5 to 20 MeV. Ann. Nucl. Energy 73, 455–464. http://dx.doi.org/10.1016/j.anucene.2014.07.023.

Dickens, J.K., 1988. SCINFUL: A Monte Carlo Based Computer Program to Determine a Scintillator Full Energy Response to Neutron Detection for E_n Between 0.1 and 80 MeV: Program Development and Comparisons of Program Predictions with Experimental Data. Technical Report, Oak Ridge National Laboratory, Oak Ridge, TN, Rep. ORNL-6463.

Eljen Technology, 2021. NEUTRON/GAMMA PSD EJ-301, EJ-309. URL: https://eljentechnology.com/products/liquid-scintillators/ej-301-ej-309.

Herman, M., Kowano, T., 2021. 181-Ta fast neutron evaluation. https://indico.bnl.gov/event/13121/contributions/57138/attachments/38417/63346/Ta181-CSEWG21.pdf.

Hutchinson, J., et al., 2024. Nuclear data sensitivity/uncertainty studies of tantalum-reflected systems. URL: https://www.osti.gov/biblio/2349298.

Iwamoto, O., et al., 2023. Japanese evaluated nuclear data library version 5: JENDL-5. J. Nucl. Sci. Technol. 60 (1), 1–60. http://dx.doi.org/10.1080/00223131.2022.2141903.

Kaschuck, Y., Esposito, B., 2005. Neutron/γ-ray digital pulse shape discrimination with organic scintillators. Nucl. Instruments Methods Phys. Res. Sect. A: Accel. Spectrometers, Detect. Assoc. Equip. 551 (2), 420–428. http://dx.doi.org/10.1016/j.nima.2005.05.071.

Knoll, G.F., 2010. Radiation Detection and Measurement. John Wiley & Sons, Inc..

Koning, A., et al., 2019. TENDL: Complete nuclear data library for innovative nuclear science and technology. Nucl. Data Sheets 155, 1–55. http://dx.doi.org/10.1016/j.nds.2019.01.002, URL: https://www.sciencedirect.com/science/article/pii/S009037521930002X Special Issue on Nuclear Reaction Data.

Lang, R., Masson, D., Pienaar, J., Röttger, S., 2017. Improved pulse shape discrimination in EJ-301 liquid scintillators. Nucl. Instruments Methods Phys. Res. Sect. A: Accel. Spectrometers, Detect. Assoc. Equip. 856, 26–31. http://dx.doi.org/10.1016/j.nima.2017.02.090, URL: https://www.sciencedirect.com/science/article/pii/S0168900217303133.

Malter, L., Langmuir, D.B., 1939. Resistance, emissivities and melting point of tantalum. Phys. Rev. 55, 743–747. http://dx.doi.org/10.1103/PhysRev.55.743.

Marrone, S., et al., 2002. Pulse shape analysis of liquid scintillators for neutron studies. Nucl. Instruments Methods Phys. Res. Sect. A: Accel. Spectrometers, Detect. Assoc. Equip. 490 (1), 299–307. http://dx.doi.org/10.1016/S0168-9002(02)01063-X.

McDermott, B.J., 2016. Resonance Region Capture Cross Section Measurements in Iron and Tantalum Using a New C_6D_6 Detector Array (Ph.D. thesis). Rensselaer Polytechnic Institute.

Meija, J., et al., 2016. Isotopic compositions of the elements 2013 (IUPAC technical report). Pure Appl. Chem. 88, 293–306. http://dx.doi.org/10.1515/pac-2015-0503.

Nobre, G., et al., 2025. ENDF/B-VIII.1: updated nuclear reaction data library for science and applications. Nucl. Data Sheets To be Published.

Overberg, M.E., et al., 1999. Photoneutron target development for the RPI linear accelerator. Nucl. Instrum. Methods Phys. Res. Sect. A 438 (2), 253–264. http://dx.doi.org/10.1016/S0168-9002(99)00878-5.

Percher, C.M., 2019. Experimental measurements summary for thermal/epithermal experiments (TEX) with ZPPR plutonium/aluminum plates with polyethylene and tantalum. http://dx.doi.org/10.2172/1532623, URL: https://www.osti.gov/biblio/1532623.

Plompen, A.J.M., et al., 2020. The joint evaluated fission and fusion nuclear data library, JEFF-3.3. Eur. Phys. J. A 56, http://dx.doi.org/10.1140/epja/s10050-020-00141-90.

Rapp, M.J., 2011. Design and Construction of a Large Area Detector System and Neutron Total Cross Section Measurements in the Energy Range 0.4 to 20 MeV (Ph.D. thesis). Rensselaer Polytechnic Institute.

Rapp, M.J., et al., 2019. Tantalum, titanium, and zirconium neutron total cross-section measurements from 0.4 to 25 MeV. Nucl. Sci. Eng. 193 (8), 903–915. http://dx.doi.org/10.1080/00295639.2019.1570750.

Rising, M.E., et al., 2023. MCNP® Code Version 6.3.0 Release Notes. Technical Report LA-UR-22-33103, Los Alamos National Laboratory, Los Alamos, NM, USA, http://dx.doi.org/10.2172/1909545.

Saglime, F.J., 2009. High Energy Nuclear Differential Scattering Measurements for Beryllium and Molybdenum (Ph.D. thesis). Rensselaer Polytechnic Institute.

Saglime, F.J., et al., 2010. A system for differential neutron scattering experiments in the energy range from 0.5 to 20 MeV. Nucl. Instrum. Methods Phys. Res. Sect. A 620 (2–3), 401–409. http://dx.doi.org/10.1016/j.nima.2010.04.051.

Sakamura, Y., et al., 1998. Measurement of standard potentials of actinides (u,np,pu,am) in licl–KCl eutectic salt and separation of actinides from rare earths by electrorefining. J. Alloys Compd. 271–273, 592–596. http://dx.doi.org/10.1016/S0925-8388(98)00166-2.

Savitzky, A., Golay, M.J.E., 1964. Smoothing and differentiation of data by simplfied least-squares procedures. Anal. Chem. 36 (8), 1627–1639. http://dx.doi.org/10.1021/ac60214a047.

Smith, A.B., Guenther, P.T., 1982. Fast-neutron scattering cross sections of elemental zirconium. http://dx.doi.org/10.2172/6486008.

Spirlet, J., et al., 1985. Direct reduction of actinide oxide and carbide to metal: Application to the preparation of plutonium metal. Nucl. Instrum. Methods Phys. Res. Sect. A 236 (3), 500–502. http://dx.doi.org/10.1016/0168-9002(85)90949-0.

Struck Innovate Systeme, 2024. SIS3305 2/4/8 channel 5/2.5/1.25 GS/S 10-bit VME digitizer. URL: https://www.struck.de/sis3305.html.

Taylor, D.F., 1999. Acid corrosion resistance of tantalum, columbium, zirconium, and titanium. Nucl. Instrum. Methods Phys. Res. Sect. A 438 (2), 253–264. http://dx.doi.org/10.1021/ie50484a023.

Wang, M., et al., 2012. The Ame2012 Atomic Mass Evaluation. Chin. Phys. C 36 (12), 1603. http://dx.doi.org/10.1088/1674-1137/36/12/003.

Youmans, A.E., et al., 2015. Fast neutron scattering measurements with lead. AccApp 15, Wash. DC 355–360.